Antiferroelectricity in lanthanum doped zirconia without metallic capping layers and post-deposition/-metallization anneals

Zheng Wang, Anthony Arthur Gaskell, Milan Dopita, Dominik Kriegner, Nujhat Tasneem, Jerry Mack, Niloy Mukherjee, Zia Karim, and Asif Islam Khan

Citation: Appl. Phys. Lett. **112**, 222902 (2018); doi: 10.1063/1.5037185

View online: https://doi.org/10.1063/1.5037185

View Table of Contents: http://aip.scitation.org/toc/apl/112/22

Published by the American Institute of Physics

APPLIED PHYSICS LETTERS **112**, 222902 (2018)

Antiferroelectricity in lanthanum doped zirconia without metallic capping layers and post-deposition/-metallization anneals

Zheng Wang,[1,a)] Anthony Arthur Gaskell,[1,a)] Milan Dopita,[2] Dominik Kriegner,[2]
Nujhat Tasneem,[1] Jerry Mack,[3] Niloy Mukherjee,[3] Zia Karim,[3] and Asif Islam Khan[1,b)]
[1]*School of Electrical and Computer Engineering, Georgia Institute of Technology, Atlanta, Georgia 30332, USA*
[2]*Department of Condensed Matter Physics, Faculty of Mathematics and Physics, Charles University, Ke Karlovu 5, CZ-121 16 Prague, Czech Republic*
[3]*Eugenus, Inc., 677 River Oaks Parkway, San Jose, California 95134, USA*

(Received 22 April 2018; accepted 15 May 2018; published online 31 May 2018)

We report the effects of lanthanum doping/alloying on antiferroelectric (AFE) properties of ZrO_2. Starting with pure ZrO_2, an increase in La doping leads to the narrowing of the AFE double hysteresis loops and an increase in the critical voltage/electric field for AFE → ferroelectric transition. At higher La contents, the polarization-voltage characteristics of doped/alloyed ZrO_2 resemble that of a non-linear dielectric without any discernible AFE-type hysteresis. X-ray diffraction based analysis indicates that the increased La content while preserving the non-polar, parent AFE, tetragonal $P4_2$/nmc phase leads to a decrease in tetragonality and the (nano-)crystallite size and an increase in the unit cell volume. Furthermore, antiferroelectric behavior is obtained in the as-deposited thin films without requiring any capping metallic layers and post-deposition/-metallization anneals due to which our specific atomic layer deposition system configuration crystallizes and stabilizes the AFE tetragonal phase during growth. *Published by AIP Publishing.* https://doi.org/10.1063/1.5037185

Antiferroelectric (AFE) oxides are an interesting class of functional materials that, under an applied electric field, undergo a first order phase transition from a non-polar parent phase into a polar ferroelectric (FE) phase and have lately been a subject of resurgent interests.[1–3] Such field-induced phase transitions lead to large changes in volume, strain, and thermal and electrical properties leading to large/giant electrostrictive, electrocaloric/pyroelectric effects and application of AFEs in high-density charge and energy storage, non-mechanical refrigeration, high performance transducers and micro-actuators, electro-optic devices, and so on.[3] Despite that, AFEs have been studied relatively less extensively compared to their close cousins: ferroelectrics—primarily because, unlike FEs which are the basis for dominant non-volatile memory technologies, AFEs do not have an intrinsic non-volatility in their polarization-electric field hysteresis characteristics. Even more so, addressing foundational aspects such as a precise definition and the origin of antiferroelectricity even in the most extensively studied AFE: lead zirconate[3,4] and search for new AFEs via high-throughput first principle calculations[3,5] happen to be rather recent developments.

That being said, what brings an unprecedented technological relevance as well as renewed scientific interests to antiferroelectricity is the recent discovery of this phenomenon in relatively simple and complementary metal-oxide-semiconductor (CMOS) compatible binary oxides based on hafnia and zirconia—concurrently with the discovery of ferroelectricity in the same.[6,7] Hafnia and zirconia have been studied extensively for microelectronic applications—specifically as high-K gate dielectrics in CMOS transistors and dynamic random-access memories. The key to this "surprising" discovery has been the use of a metallic capping layer and post-metallization anneal in N_2. These specific processing conditions lead to a partial or complete suppression of the bulk ground state: non-polar monoclinic phase (space group $P2_1/c$, #14) in favor of a non-polar, tetragonal phase (space group $P4_2/nmc$, #137), which we will refer to as the parent AFE phase in the rest of the letter. Under an applied electric field, the parent AFE, tetragonal phase transforms through a first order phase transition into a polar FE phase with an orthorhombic structure (space group $Pca2_1$, #29).[8] Interestingly, it has recently been demonstrated that these new AFEs can not only be used as non-volatile memory elements—the main-stay for applications of FEs—but also with a much improved cycling endurance and stability compared to FEs, the key being work-function and interfacial layer engineering.[9–12] AFEs can also be utilized for ultra-low power logic applications by exploiting their negative capacitance properties.[13] As such, the scope of these CMOS compatible AFEs goes far beyond traditional applications of antiferroelectricity[14–16] and have the potential to disrupt the microelectronics industry and computing.

To stabilize and tailor ferroelectric properties in HfO_2, the role of doping and compositional tuning have been proven to be of critical importance. A wide variety of chemical elements such as Si,[7] Al,[15,17] Zr,[6,14] Sr,[18] Sc,[19] La,[20] Gd,[21] Nb,[22] Y,[23] Mg,[18] Ge,[22] and N[22] have been explored as dopants in HfO_2 to find the ideal one with respect to the robustness of the ferroelectricity, CMOS compatibility, the process window, as well as specific applications such as in actuators, piezo-electric, pyroelectric, and electro-caloric devices. On the other hand, in the case of their antiferroelectric counterparts, these types of studies have been rather limited; antiferroelectricity in $Hf_xZr_{1-x}O_2$[6] and Si and Al doped HfO_2[7,17,24] and $Hf_{0.5}Zr_{0.5}O_2$[16] have been investigated so far. Towards that end, we consider the fluorite-type prototypical antiferroelectric: ZrO_2, and study the effects

---

[a)] Z. Wang and A. Gaskell contributed equally to this work.
[b)] asif.khan@ece.gatech.edu

of La doping/alloying on its antiferroelectric properties through a combined electrical and X-ray diffraction (XRD) based structural investigation in this letter. It is observed that with the increase in La content, the antiferroelectric double hysteresis loop becomes narrower and the critical field for AFE → FE transition increases. At high La contents, the polarization vs. electric field curves of ZrO_2 resemble those of a non-linear dielectric devoid of any discernible AFE-type hysteretic characteristics. Such evolution of the electrical properties correlates well with the observations from the X-ray diffraction measurement that with an increasing La content, the reflections from parent AFE phase (tetragonal $P4_2/nmc$ structure) become weaker, the tetragonality and the (nano-)crystallite size decrease and the corresponding unit cell volume increases. We also report that it is possible to stabilize robust antiferroelectricity in ZrO_2 and its doped/alloyed variants without requiring any capping metallic layer and post-deposition and post-metallization rapid thermal annealing in N_2.

Thin films of ZrO_2 and its La-doped/alloyed variants were deposited using thermal atomic layer deposition (ALD) technique in a Eugenus QXP mini-batch 300 mm ALD system with cyclopentadienyl (Cp) complexes used as precursors for ZrO_2 and La_2O_3. ALD deposited TiN (10 nm) was used as the bottom electrode, and no top TiN layer was deposited. The deposition temperature was kept at 400 °C. The La content was adjusted by varying the ratio of La_2O_3 cycles to ZrO_2 cycles. Taking into account the deposition rates of ZrO_2 and La_2O_3, the total number of cycles was adjusted such that the thickness of the oxide layer was 10 nm which was also confirmed by the X-ray reflectivity measurements (supplementary material, Fig. S1). Sputter deposited Ti(5 nm)/Au(60 nm) metal layers patterned into square shapes were used as top electrodes. We did not perform any rapid thermal annealing—neither post-deposition nor post-metallization—of the samples. X-ray photoelectron spectroscopy technique was used to estimate the atomic La content in these samples. In the rest of the letter, La contents in the doped/alloyed ZrO_2 samples are given as % of cationic fraction of La, which we define as $[La]/([La] + [Zr]) \times 100$.

Figures 1(a) and 1(b) show the polarization P-voltage V(electric field E) characteristics and the dielectric constant ϵ_r–$V(E)$ characteristics, respectively, in pure ZrO_2 and its La doped variants. Also plotted in Fig. 1(a) are the corresponding transient switching current I_{sw}-$V(E)$ characteristics. In the $P-E$ and $I_{sw}-E$ curves for doped ZrO_2 in Fig. 1(a), the corresponding curves for pure ZrO_2 are also plotted in the background in dotted lines to provide a comparison. The $P-V\ (E)$ and $\epsilon_r-V\ (E)$ characteristics for other La contents are shown in supplementary material Fig. S2. The $P-V$ hysteresis measurements were performed using a aixACCT TF-3000 ferroelectric parameter analyzer at a frequency of 1 kHz with the dynamic leakage compensation enabled.[25] The capacitance measurements were performed using an impedance analyzer (E4990A) at a frequency of 100 kHz. For each sample during polarization and capacitance measurement, the voltage sweep range was maximized under the constraint that the peak voltages do not cause a film break-down.

In Fig. 1(a), the $P-V(E)$ curves for pure ZrO_2 and ZrO_2 with up to 3.5% of La content have a double hysteresis shape which is characteristic of antiferroelectric oxides. The $I_{sw}-V(E)$ characteristics of these samples have four well-separated peaks, which correspond to the steepest points in the $P-V(E)$ curves indicated by the arrow in Fig. 1(a) further confirming their double hysteresis shape. The antiferroelectric hysteresis loops in all four of these samples are retained after cycling up to at least 10^7–10^8 cycles at 100 kHz at the same peak voltages which indicates that the double loop feature is not due to any defect mediated mechanisms and, hence, confirms the antiferroelectric nature of these films. In line with this observation, the dielectric constant-electric field characteristics in these four films as shown in Fig. 1(b) also have the antiferroelectric double butterfly shape—i.e., the dielectric constant shows two peaks for each sweep direction with the peaks shifted relative to each other for different sweep directions. We note in Fig. 1(a) that the antiferroelectric hysteresis loops are asymmetric—i.e., the loop in the first quadrant in the P–V coordinate system is wider than that in the third quadrant. This asymmetry is possibly due to the asymmetry of the ALD grown structure, which has a bottom TiN layer but not a top one. Such asymmetry in the hysteresis loop is not observed in symmetric structure: TiN/ZrO_2/TiN on Si grown using the ALD technique (see supplementary material, Fig. S4).

To obtain a better understanding of the evolution of AFE characteristics with La doping, Fig. 2(a) shows how the maximum width of the hysteresis window in the first quadrant of the $P-V$ characteristics shown in Fig. 1(a) changes as a function of La content. Figure 2(b) plots the evolution of the voltage corresponding to the peak switching current in the first quadrant loop [denoted by P in Fig. 1(a)], V_P, as a function of La content. Figures 1(a), 2(a), and 2(b) show that with the increase in La content up to 3.5%, the hysteresis loops become narrower, critical voltages and electric fields required for AFE → FE transition increases, and the loops shift to higher voltages/electric fields. Similar behavior is observed in Fig. 2(c), which plots the voltage corresponding to the peak in ϵ_r–V characteristics [noted as P′ in Fig. 1(b)] as a function of La content. For La content $\geq$5.4%, the loop ceases to exist for applied voltage range, which is also corroborated by the non-existence of the peaks in $I_{sw}-V(E)$ and $\epsilon_r-V(E)$ characteristics in corresponding doped/alloyed ZrO_2 samples shown in Figs. 1(a) and 1(b), respectively.

The X-ray diffraction (XRD) analysis was performed to obtain insights into the phase composition and structural and microstructural information about the (nano-)crystalline phases in these thin films. The details of XRD measurement protocol are provided in the supplementary material. In Fig. 3(a), the measured glancing incidence X-ray diffraction (GI-XRD) patterns of the samples as deposited are shown. For reference, the diffraction peak positions of the tetragonal $P4_2/nmc$, orthorhombic $Pca2_1$, and monoclinic $P2_1/c$ phases are marked in Fig. 3(a). We observe that the Bragg peaks for pure ZrO_2 and ZrO_2 with low La content match well with those of the tetragonal structure. No resemblance of the diffraction patterns of our samples with the orthorhombic and monoclinic patterns is observed in these samples indicating that the crystalline phase in these samples are predominantly or fully tetragonal with non-existing or extremely tiny fractions (below the detection limit of our XRD set-up) of orthorhombic and monoclinic phases. With the increase in La content, the peaks become

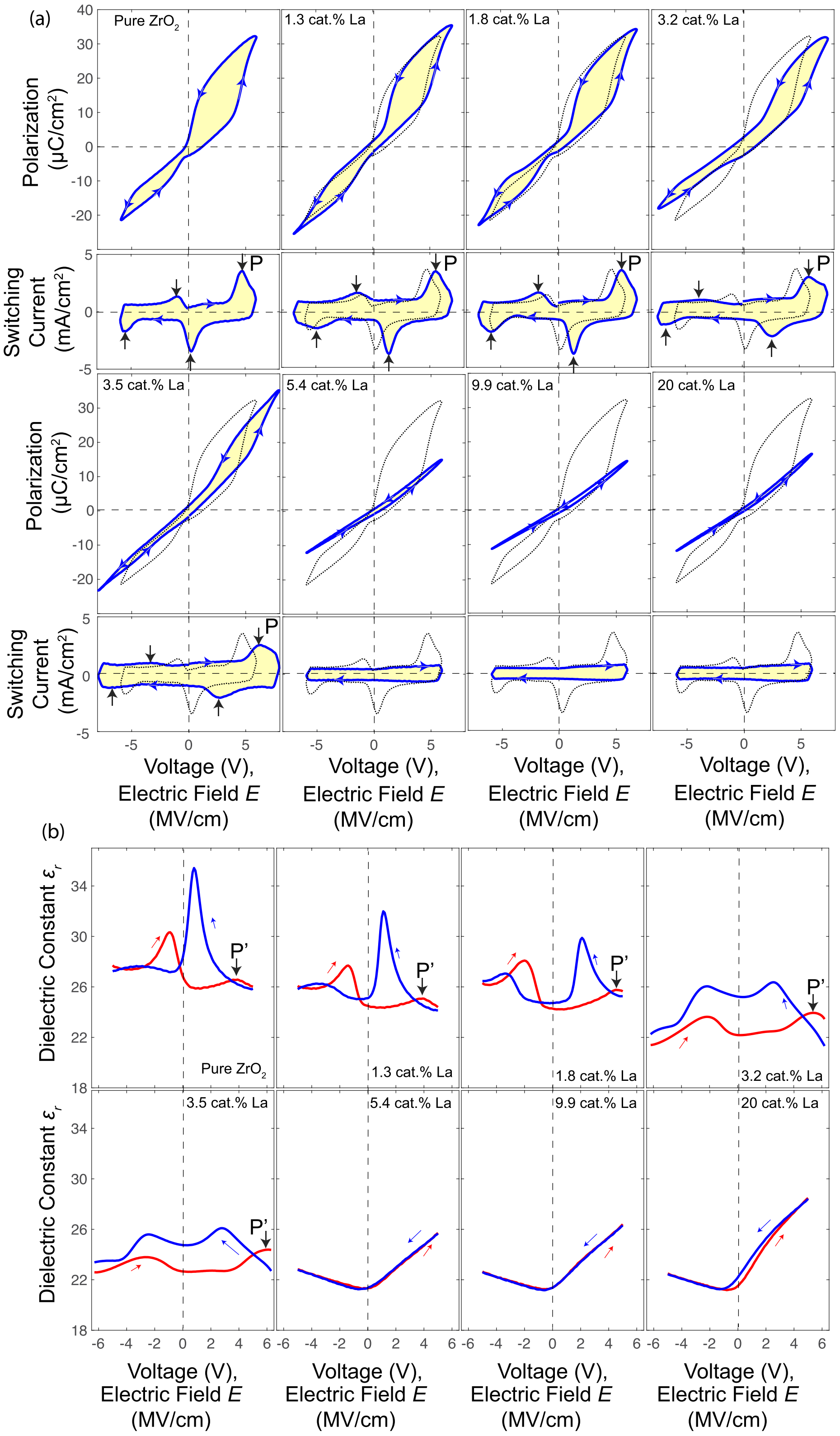

FIG. 1. The evolution of the polarization-voltage/electric field hysteresis curves and switching current-voltage/field characteristics (a) and dielectric constant-voltage/electric field characteristics (b) as La content level is changed from 0 (pure ZrO_2) to 20%. In the $P-E$ and $I_{sw}-E$ curves for doped ZrO_2 in Fig. (a), the corresponding curves for pure ZrO_2 are also plotted in the background in dotted lines to provide a comparison.

weaker, and for %La content ≥9.9%, the XRD pattern cannot be distinguished as diffraction patterns from any of the aforementioned structures. In addition, extremely broadened peaks are also observed—most clearly in samples with highest La content—in Fig. 3(a) indicated by * which correspond to a phase with extremely small crystallites, or nearly amorphous phase embedding the crystals of tetragonal phase. Given that the tetragonal $P4_2/nmc$ structure is the parent AFE phase, the overall decrease in XRD signal from the tetragonal crystal with increasing La content is consistent with the observed evolution of AFE characteristics shown in Fig. 1(a)—particularly the absence of AFE behavior in the high La content ZrO_2 samples.

The critical field for AFE → FE transition depends on crystallographic and micro-structural details among many other effects.[20,26,27] Figures 3(b)–3(d) plot the evolution of refined lattice parameters a and c and the tetragonality (c/a^*) of the tetragonal structure, respectively, with respect to the

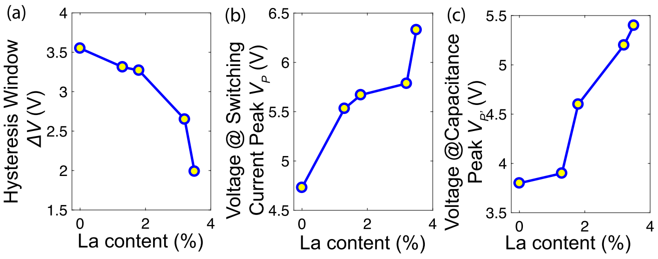

FIG. 2. The evolution of the hysteresis window (a), voltage at peak switching current V_P (b) and voltage at peak capacitance $V_{P'}$ with respect to La content (c).

La content. The lattice parameters of crystalline phases and sizes of the coherently diffracting domains—crystallite sizes were obtained by the fitting of measured diffraction patterns using the MStruct software. Measured diffraction patterns were fitted using the whole powder pattern refinement method (Rietveld method).[28] In calculating the tetragonality (c/a^*), the a-parameters plotted in Fig. 3(b) were recalculated into "cubic" axes (i.e., $a^* = a\sqrt{2}$). In pure ZrO_2, we observe $(a, c) \equiv (\sim 3.595\,\text{Å}, \sim 5.19\,\text{Å})$, which is in a good agreement with lattice parameters reported in Ref. 6. It is observed in Figs. 3(b)–3(d) that a increases while c decreases decreasing the tetragonality (c/a) with the increase in La content, suggesting that La doping/alloying has an effect similar to that of a bi-axial tensile strain in the tetragonal basal plane of ZrO_2 nano-crystallites. Note that similar suggestion was made for the case of La doped HfO_2 in Ref. 20 albeit on its orthorhombic $Pca2_1$ phase. Figure 3(d) shows that with the increase in La content, the tetragonal unit cell volume increases which is expected since the ionic radius of La^{3+} (116 pm) is much larger than that of Zr^{4+} (80 pm).[20,29] In addition, we note in Fig. 3(a) that with increasing La content, the peaks of tetragonal phase become broadened, which is the indication for decrease in the crystallite size. This is confirmed by the evolution of the refined mean size of the coherently diffracting domains—i.e., the mean size of the nanocrystallites—of tetragonal phase with respect to the La content shown in Fig. 3(d). By correlating the XRD data shown in Figs. 3(b)–3(f) and the electrical data shown in Figs. 1 and 2, we conclude that the increase in La content via its influence on the tetragonal lattice parameters and nanocrystallite size increases the energy difference between the non-polar AFE tetragonal and the polar FE orthorhombic phases resulting in the increase in the critical field for AFE → FE transition.

It is interesting to note that the diffraction patterns of ZrO_2 with 4.5% and 5.4% La content show discernible tetragonal reflections [see Fig. 3(a)] while the $P-V$ characteristics of the corresponding samples do not show a double hysteresis loop—rather, they resemble a non-linear dielectric-like behavior. However, the refined lattice parameters of this phase in these two samples are subjected to relatively high errors [see the errorbars in Figs. 3(b) and 3(c)] owing to the peaks from tetragonal phase being very broad and weak [see Fig. 3(a)]. This suggests the possibility that the critical field for AFE → FE transition in these two samples may be higher than the break down voltage. Further analyses based on electrical and detailed structural characterization combined with first-principle calculations can shed more light into a complete picture of the evolution of AFE characteristics in doped ZrO_2 antiferroelectrics.[8,20,26,27,30,31]

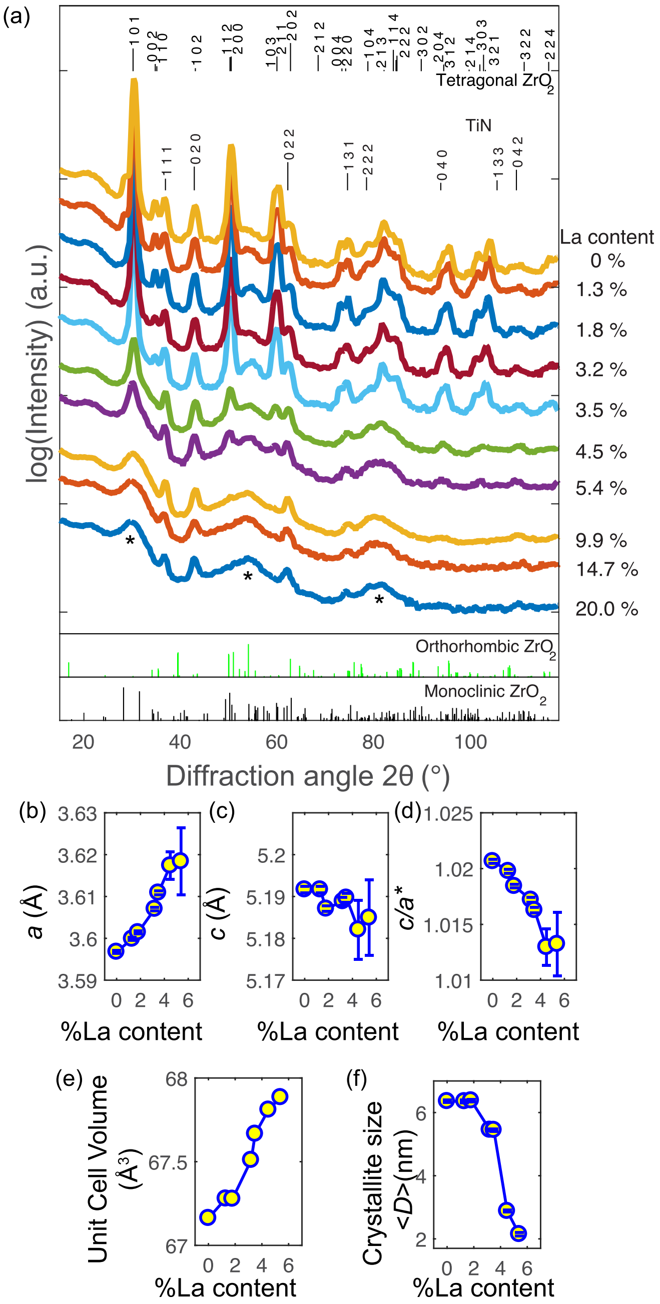

FIG. 3. (a) Measured grazing-incidence X-ray diffraction patterns of ZrO_2 and its doped/alloyed variants. The positions of diffraction peaks and its indices for tetragonal ZrO_2 and TiN phases are marked at the top of the figure. For comparison, the position of the diffraction peaks of orthorhombic ZrO_2 and monoclinic ZrO_2 are indicated at the bottom. *'s indicate peaks corresponding to a highly nanocrystalline or nearly x-ray amorphous phase. (b)–(f) The evolution of the lattice parameters a (b) and c (c), tetragonality (c/a^*) (d), tetragonal unit cell volume (e) and the coherently diffracting domain size (nano-crystallite size) of the tetragonal phase (f) as a function of La content. In calculating the tetragonality (c/a^*) for (d), the a-parameters plotted in (b) were recalculated into "cubic" axes $\left(i.e., a^* = a\sqrt{2}\right)$.

Rapid thermal annealing typically at a temperature range of 400–900 °C for 1–30 s in the presence of a top metallic capping layer (such as TiN,[6,7,21,32] TaN,[21] Ir,[33–35] Pt,[36,37] W,[38] and RuO_2[39]) in N_2 ambient [generally referred to as post-metallization annealing (PMA)] has been shown to be critical to stabilize the robust ferroelectric and the antiferroelectric properties in HfO_2 and ZrO_2 based oxides. Annealing without a capping layer in N_2 ambient [referred to as post-deposition anneal (PDA)] at 500–900 °C for 20–30 s can also stabilize the same in doped/alloyed HfO_2 and $Hf_xZr_{1-x}O_2$ in Refs. 16, 19, and 22. For both these instances of PMA and PDA, the as-deposited films were amorphous since the substrate temperature was kept at relatively low temperatures (200–280 °C) during the ALD. In our case, the observed reflections in the XRD pattern of the as-deposited films shown in Fig. 3(a) confirm that our films of ZrO_2 and its doped/alloyed variants crystallized into the tetragonal ($P4_2/nmc$) AFE (nano-)crystalline phase during the ALD without requiring a capping layer and a PMA/PDA in N_2 ambient. In addition to a relatively higher deposition temperature (400 °C) due to cyclopentadienyl (Cp) based precursors, Eugenus QXP ALD system also employs TriJet Vaporizer for precursor delivery in a small volume reaction space. Specific QXP ALD system configuration (i.e., 400 °C) coupled with vaporization of precursors may be responsible for as-deposited tetragonal crystalline phase of ZrO_2 and its doped/alloyed variants.

In summary, we reported the tunability of antiferroelectric properties of ZrO_2 through La doping/alloying. As we move from pure ZrO_2 to ZrO_2 with small La content, the antiferroelectric double hysteresis loops become narrower, critical voltages and electric fields required for AFE → FE transition increases, and the loops shift to higher voltages/electric fields. At high La content, the films behave as non-linear dielectric without any discernible AFE-like hysteresis. The evolution of electrical properties is correlated with the weakening of tetragonal $P4_2/nmc$ reflections from parent AFE phase and a characteristics change in the unit cell parameters and (nano-)crystallite size with increasing La content. Furthermore, we show that specific ALD configuration can stabilize antiferroelectricity in as-grown pure and doped/alloyed ZrO_2 without requiring any metallic capping layer and post-deposition/-metallization anneals.

See supplementary material for details on glancing incidence X-ray diffraction procedure, thickness measurement, and the dielectric constant measurement.

This work was supported in part by the National Science Foundation (Grant No. 1718671). This work was performed in part at the Georgia Tech Institute for Electronics and Nanotechnology, a member of the National Nanotechnology Coordinated Infrastructure, which is supported by the National Science Foundation (Grant No. ECCS-1542174). M.D. and D.K. are thankful to NanoCent-Nanomaterials Centre for Advanced Applications (Project No. CZ.02.1.01/0.0/0.0/15_003/0000485) financed by ERDF. A.I.K. is thankful to M. Hoffmann for useful insights.

[1] G. Shirane, E. Sawaguchi, and Y. Takagi, Phys. Rev. **84**, 476 (1951).
[2] C. Kittel, Phys. Rev. **82**, 729 (1951).
[3] K. M. Rabe, *Functional Metal Oxides: New Science and Novel Applications* (Wiley-VCH Verlag GmbH & Co. KGaA, 2013), pp. 221–244.
[4] P. Tolédano and M. Guennou, Phys. Rev. B **94**, 014107 (2016).
[5] J. W. Bennett, K. F. Garrity, K. M. Rabe, and D. Vanderbilt, Phys. Rev. Lett. **110**, 017603 (2013).
[6] J. Müller, T. S. Boscke, U. Schroeder, S. Müller, D. Brauhaus, U. Bottger, L. Frey, and T. Mikolajick, Nano Lett. **12**, 4318 (2012).
[7] T. Böscke, S. Teichert, D. Bräuhaus, J. Müller, U. Schröder, U. Böttger, and T. Mikolajick, Appl. Phys. Lett. **99**, 112904 (2011).
[8] S. E. Reyes-Lillo, K. F. Garrity, and K. M. Rabe, Phys. Rev. B **90**, 140103 (2014).
[9] M. Pešić, M. Hoffmann, C. Richter, T. Mikolajick, and U. Schroeder, Adv. Funct. Mater. **26**, 7486 (2016).
[10] M. Pešić, S. Knebel, M. Hoffmann, C. Richter, T. Mikolajick, and U. Schroeder, in *2016 IEEE International Electron Devices Meeting (IEDM)* (IEEE, 2016), pp. 11–16.
[11] M. Pešić, T. Li, V. D. Lecce, M. Hoffmann, M. Materano, C. Richter, B. Max, S. Slesazeck, U. Schroeder, L. Larcher *et al.*, J. Electron Devices Soc. (published online, 2018).
[12] M. Pešić, U. Schroeder, S. Slesazeck, and T. Mikolajick, IEEE Trans. Devices Mater. Reliab. (published online, 2018).
[13] M. Lee, Y.-T. Wei, K.-Y. Chu, J.-J. Huang, C.-W. Chen, C.-C. Cheng, M.-J. Chen, H.-Y. Lee, Y.-S. Chen, L.-H. Lee *et al.*, IEEE Electron Device Lett. **36**, 294 (2015).
[14] M. H. Park, H. J. Kim, Y. J. Kim, T. Moon, K. Do Kim, and C. S. Hwang, Nano Energy **12**, 131 (2015).
[15] M. H. Park, T. Schenk, M. Hoffmann, S. Knebel, J. Gärtner, T. Mikolajick, and U. Schroeder, Nano Energy **36**, 381 (2017).
[16] P. D. Lomenzo, C.-C. Chung, C. Zhou, J. L. Jones, and T. Nishida, Appl. Phys. Lett. **110**, 232904 (2017).
[17] S. Mueller, J. Mueller, A. Singh, S. Riedel, J. Sundqvist, U. Schroeder, and T. Mikolajick, Adv. Funct. Mater. **22**, 2412 (2012).
[18] S. Starschich and U. Boettger, J. Mater. Chem. C **5**, 333 (2017).
[19] L. Xu, T. Nishimura, S. Shibayama, T. Yajima, S. Migita, and A. Toriumi, Appl. Phys. Express **9**, 091501 (2016).
[20] U. Schroeder, C. Richter, M. H. Park, T. Schenk, M. Pešić, M. Hoffmann, F. P. Fengler, D. Pohl, B. Rellinghaus, C. Zhou *et al.*, Inorg. Chem. **57**, 2752 (2018).
[21] M. Hoffmann, U. Schroeder, T. Schenk, T. Shimizu, H. Funakubo, O. Sakata, D. Pohl, M. Drescher, C. Adelmann, R. Materlik *et al.*, J. Appl. Phys. **118**, 072006 (2015).
[22] L. Xu, T. Nishimura, S. Shibayama, T. Yajima, S. Migita, and A. Toriumi, J. Appl. Phys. **122**, 124104 (2017).
[23] J. Müller, U. Schröder, T. Böscke, I. Müller, U. Böttger, L. Wilde, J. Sundqvist, M. Lemberger, P. Kücher, T. Mikolajick *et al.*, J. Appl. Phys. **110**, 114113 (2011).
[24] M. Hoffmann, T. Schenk, M. Pešić, U. Schroeder, and T. Mikolajick, Appl. Phys. Lett. **111**, 182902 (2017).
[25] R. Meyer, R. Waser, K. Prume, T. Schmitz, and S. Tiedke, Appl. Phys. Lett. **86**, 142907 (2005).
[26] M. Pešić, F. P. G. Fengler, L. Larcher, A. Padovani, T. Schenk, E. D. Grimley, X. Sang, J. M. LeBeau, S. Slesazeck, U. Schroeder *et al.*, Adv. Funct. Mater. **26**, 4601 (2016).
[27] E. D. Grimley, T. Schenk, T. Mikolajick, U. Schroeder, and J. M. LeBeau, Adv. Mater. Interfaces **5**, 1701258 (2018).
[28] Z. Matěj, A. Kadlecová, M. Janeček, L. Matějová, M. Dopita, and R. Kužel, Powder Diffr. **29**, S35 (2014).
[29] R. D. Shannon, Acta Crystallogr. Sect. A: Cryst. Phys., Diffr., Theor. Gen. Crystallogr. **32**, 751 (1976).
[30] R. Batra, T. D. Huan, G. A. Rossetti, Jr., and R. Ramprasad, Chem. Mater. **29**, 9102 (2017).
[31] R. Materlik, C. Künneth, and A. Kersch, J. Appl. Phys. **117**, 134109 (2015).
[32] M. Hyuk Park, H. Joon Kim, Y. Jin Kim, W. Lee, T. Moon, and C. Seong Hwang, Appl. Phys. Lett. **102**, 242905 (2013).
[33] M. H. Park, H. J. Kim, Y. J. Kim, W. Lee, T. Moon, K. D. Kim, and C. S. Hwang, Appl. Phys. Lett. **105**, 072902 (2014).
[34] P. D. Lomenzo, P. Zhao, Q. Takmeel, S. Moghaddam, T. Nishida, M. Nelson, C. M. Fancher, E. D. Grimley, X. Sang, J. M. LeBeau *et al.*, J. Vac. Sci. Technol. B **32**, 03D123 (2014).
[35] T. Shimizu, T. Yokouchi, T. Shiraishi, T. Oikawa, P. S. R. Krishnan, and H. Funakubo, Jpn. J. Appl. Phys., Part 1 **53**, 09PA04 (2014).
[36] S. Starschich, D. Griesche, T. Schneller, R. Waser, and U. Böttger, Appl. Phys. Lett. **104**, 202903 (2014).
[37] M. Hyuk Park, H. Joon Kim, Y. Jin Kim, W. Lee, H. Kyeom Kim, and C. Seong Hwang, Appl. Phys. Lett. **102**, 112914 (2013).
[38] G. Karbasian, R. dos Reis, A. K. Yadav, A. J. Tan, C. Hu, and S. Salahuddin, Appl. Phys. Lett. **111**, 022907 (2017).
[39] M. H. Park, H. J. Kim, Y. J. Kim, W. Jeon, T. Moon, and C. S. Hwang, Phys. Status Solidi (RRL) **8**, 532 (2014).